An Infrared Transmission Study of Ge:Mn Thick Films Prepared by Ion Implantation and Post-Annealing

Obied, L. H.; Roorda, S.; Prucnal, S.; Zhou, S.; Crandles, D. A.;

Originally published:

March 2020

Journal of Applied Physics 127(2020), 103902

DOI: https://doi.org/10.1063/1.5143249

An Infrared Transmission Study of Ge:Mn Thick Films Prepared by Ion Implantation and Post-Annealing

L. H. Obied,[1] S. Roorda,[2] S. Prucnal,[3] Shenqiang Zhou,[3] and D.A. Crandles[1]
[1)] *Dept. of Physics, Brock University, St. Catharines, ON, L2S 3A1 Canada*
[2)] *Dept. de Physique, U. de Montréal, Montréal, PQ, H3T 1J4 Canada*
[3)] *Institute of Ion Beam Physics and Materials Research, Helmholtz-Zentrum, Dresden-Rossendorf, PO Box 510119, Dresden 01314, Germany*

(Dated: 21 February 2020)

Ge:Mn thick films (t≈ 3μm) with low average Mn concentration (< 0.3%) were prepared by ion implantation at 77K followed by either conventional or flash lamp annealing. The films were characterized by Xray diffraction, Secondary Ion Mass Spectrometry, magnetometry and infrared transmission (100-6500 cm^{-1}). Post-annealing at high enough temperature recrystallizes the amorphous Ge:Mn films without significant migration of Mn to the surface while solid phase epitaxy does not occur, resulting in polycrystalline films. Annealing causes an estimated 50-80% of the implanted Mn to migrate to Mn-rich clusters or form Mn_5Ge_3 while the remainder enters the Ge lattice substitutionally creating free holes. Evidence for free holes comes from structure in the mid-infrared absorption coefficient that is similar to previous observations in p-type Ge. The data suggest that the maximum solubility of Mn in the Ge crystalline lattice has an upper limit of < 0.08%.

PACS numbers: 75.50.Pp,78.20.Ci,78.20.-e,81.05.Hd
Keywords: magnetic semiconductors, infrared spectroscopy, ion implantation, annealing

I. INTRODUCTION

The first report[1] of ferromagnetism in manganese-doped Germanium (Ge:Mn) opened a period of intense research into this interesting system. When the studies began in the early 2000's it was hoped that uniformly doped Ge:Mn could be prepared and it would be a dilute magnetic semiconducting system (DMS) compatible with silicon based technology. However, if Molecular Beam Epitaxy (MBE) was used to grow $Ge_{1-x}Mn_x$ films ($0.01 \leq x \leq 0.1$), Mn-rich precipitates such as Mn_5Ge_3 or $Mn_{11}Ge_8$ formed easily if the substrate temperature (T_s) was greater than 80°C, and at even lower T_s if the growth rate was too quick[2]. While no precipitates formed if $T_s < 60$°C during MBE, it was found that the resulting Mn concentration was still not homogeneous. However, instead of Mn_5Ge_3 precipitates, amorphous Mn-rich clusters were observed which have large moments and exhibit ferromagnetism for $T < 15$K[3,4].

Several groups employed ion implantation as an alternative to MBE in the hope of fabricating uniformly doped Ge:Mn but found that if the target temperature was held high to avoid amorphization ($T_s > 300$°C), Mn_5Ge_3 inclusions again formed[5,6]. On the other hand, if the target temperature was kept at 77K, the films were free of inclusions and were ferromagnetic at low temperature[7] as long as the average implanted Mn concentration was less than 3%. It was also determined that pulsed laser post-annealing after ion implantation was more effective in producing free holes (and substitutional Mn, presumably) than ion implantation alone using high target temperature[8,9].

Later still, the maximum solubility of Mn in Ge was estimated to be approximately 0.7-0.9% by means of experiments in which changes in the depth profile of Mn were measured as function of annealing temperature and duration[10]. At around the same time, Ge:Mn films with ultralow Mn concentration (≈0.25%) were fabricated by MBE ($T_s = 95$°C) and it was determined that films were free of precipitates yet ferromagnetic[11].

The idea for the present study is based on previous work on Mn ion-implanted InP and GaP (average Mn concentration ≈ 2.5%) that was further processed by rapid thermal annealing (RTA)[12]. It was found that RTA induced solid phase epitaxy (SPE) which is the process in which a crystalline substrate layer below an amorphous layer provides a template for reconstruction via annealing[13]. During annealing, a thermally activated crystalline-amorphous (c-a) interface moves as the amorphous layer recrystallizes. In the aforementioned InP:Mn and GaP:Mn samples, it was shown that Mn atoms in excess of the solubility limit were squeezed out of the growing epitaxial layer of maximum Mn concentration while an amorphous highly Mn-rich layer containing MnP inclusions built up in front of the moving c-a interface[12]. In the present work, the idea was to produce Ge:Mn layers with Mn-concentration below the solubility limit[10] estimated by Portavoce *et al.* and then employ various post-annealing methods in the hope of producing epitaxial Ge:Mn via SPE without inclusions or Mn-rich clusters.

The samples were characterized by Xray diffraction (XRD), Secondary Ion Mass Spectrometry (SIMS), magnetometry and far- to mid- infrared (MIR,FIR) transmission spectroscopy (100-7000 cm^{-1}). FIR spectroscopy provides a contact free method to simultaneously determine the density of free holes and their mobility and can provide insight as to the position of the Fermi level and whether the holes are moving in an impurity band, or one of the valence bands of crystalline Ge. Previous infrared transmission measurements made on amorphous Ge:Mn[14] films prepared by radio frequency (RF) sputtering detected a broadened fundamental band absorption edge in the narrow frequency range (4400-7000 cm^{-1}).

Infrared spectroscopy was used extensively to characterize the dilute magnetic semiconductor GaAs:Mn which permits a relatively high degree of Mn substitution and contributed to the discussion on whether the Fermi level was in the valence band or in the middle of an impurity band[15,16].

As will be seen below, annealing causes the Ge:Mn thick layers to become inhomogeneous. The combination of magnetometry and infrared transmission measurements proved able to determine the fraction of Mn entering the dilute Ge:Mn matrix and the fraction entering Mn rich clusters. It will be shown that the data can be understood if there are multiple phases consisting of Mn_5Ge_3 or Mn-rich nanoparticles in a background Ge matrix containing magnetically isolated Mn atoms and that the number of dispersed Mn ions is of the same order of magnitude as the number that enter Mn-rich nanoparticles. This is in contrast to earlier work on post-annealing of ion implanted samples with ≈ 10% Mn doping where the highest hole density produced by post-annealing was two orders of magnitude lower than the average implanted Mn concentration[9].

II. SAMPLE PREPARATION

Nearly intrinsic single crystalline (100) Ge substrates with high resistivity (ρ >40 Ω-cm) were held at liquid nitrogen temperature while implanting three different ways: a single implantation using either Mn^{2+} or Ge^{2+} ions, or a multiple implantation using only Mn^{2+} ions. The single implantations used ion energy of 4.76 MeV and fluence 2×10^{16} cm^{-2} (which is above the amorphization threshold) to achieve a skewed Gaussian distribution of implanted ions with a projected range of about 2.25 μm. The multiple implantation of Mn^{2+} was done with four different ascending ion energies to extend the implanted region towards the surface with pairs of energies and fluence as follows (4.76 MeV, 4.5×10^{15} cm^{-2}), (2.7 MeV, 3×10^{15} cm^{-2}), (1.5 MeV, 1.75×10^{15} cm^{-2}), (800 keV, 7.5×10^{14} cm^{-2}). The total fluence for the multiple implantation was 1×10^{16} cm^{-2} which was also above the amorphization threshold.

The implantation schemes have been chosen to produce relatively thick (approximately 1% of the total substrate thickness) amorphous Ge (aGe) or Ge:Mn films that satisfy three properties: a large enough total magnetic moment for good quality magnetometry signal while maintaining average Mn concentration below the 0.7-0.9% solubility limit[10] and a thickness that enlarges the effect of film absorption on the transmission of the two-layer film/substrate structures.

After each kind of implantation, the implanted substrate was cut using a diamond scribe into a group of small samples of size about 5 × 5 mm (mass ≈50 mg). Conventional annealing was performed using a single-zone tube furnace at either 200 °C or 330 °C for 168 hours and 33 hours, respectively. The annealing durations were chosen using the thermally activated speed of the moving crystalline/amorphous interface in ion-implanted aGe[13]. On some samples, flash lamp annealing (FLA) was performed at energy density of 41 J/cm^2 for duration of 3 ms instead of conventional annealing. The implanted layers were placed away from the flash lamp so that thermal energy initially flowed from the crystalline substrate towards the amorphous layer. Samples were handled throughout preparation and all measurements with Teflon tweezers to avoid contamination with magnetic particles[17]. Table I lists a description of the preparation conditions for all the samples studied in this work.

TABLE I. List of samples. Sample labels are composed of two parts: implantation_annealing. The three implantation labels are aGe (Ge single implantation which produces amorphous Ge), SI (Mn single implantation) and MI (Mn multiple implantation). See text for implantation details. The four annealing labels are NA (no annealing), C200 (conventional at 200°C), C330 (conventional at 330°C) and FLA (flash lamp annealing).

Sample ID	Annealing Type	Annealing parameters	Annealing Duration
Self Implantation: Ge^{2+} fluence 2×10^{16}/cm^2			
aGe_NA	none	-	
aGe_C330	conventional	330 °C	33 h
aGe_FLA	Flash Lamp	41 J/cm^2	3 ms
Single Implantation Mn^{2+} fluence: 2×10^{16}/cm^2 Average Mn concentration 0.23%			
SI_NA	none	-	
SI_C200	conventional	200 °C	168 h
SI_C330	conventional	330 °C	33 h
SI_FLA	Flash Lamp	41 J/cm^2	3 ms
Mulitiple Implantation: total Mn^{2+} fluence: 1×10^{16}/cm^2 Average Mn concentration 0.08%			
MI_NA	none	-	
MI_C200	conventional	200 °C	168 h
MI_C330	conventional	330 °C	33 h
MI_FLA	Flash Lamp	41 J/cm^2	3 ms

III. STRUCTURAL CHARACTERIZATION

The crystallinity of the thick films was studied by XRD using a Rigaku Smartlab (40kV,40mA,Cu radiation) system. In addition SIMS analyses were made at Surface Science Western to determine the Mn depth profile. The samples were analysed with a Cameca IMS-6f ion microprobe using a positive oxygen beam and monitoring various positive secondary ions of interest. The depth scales were obtained by measuring the SIMS craters with a Tencor P10 surface profilometer.

SPE was investigated in self amorphized Ge (a-Ge) thick films using conventional annealing and FLA. In Fig. 1, the XRD pattern of the virgin substrate exhibits only the (400) Bragg peak while the self-implanted but not annealed substrate (aGe_NA) exhibits two very broad peaks centered at around 27° and 50° in Fig. 1. The difference shows that the unannealed thick layer is amorphous. Af-

ter conventional annealing at 330 °C, (aGe_C330) the broad peaks in the XRD pattern of sample aGe_C330 disappear leaving only the (400) peak, suggesting that the amorphous layer was recrystallized via SPE. On the other hand, the XRD pattern of sample aGe_FLA shows peaks corresponding to polycrystalline Ge. It is curious that the forbidden (200) peak appears in sample aGe_FLA in Fig.1. It is also observed in some of the Ge:Mn films, as will be seen below, but not all of them. Its appearance is very difficult to explain except to note that (200) peaks have been observed previously in some measurements on Ge single crystals and attributed to multiple reflection effects[18].

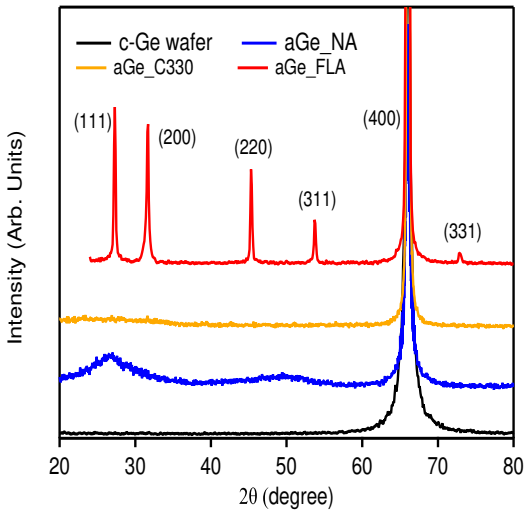

FIG. 1. (Colour Online) XRD patterns of self-implanted samples before (aGe_NA) and after conventional (aGe_C330) and flash lamp annealing (aGe_FLA) compared with virgin (100) Ge substrate

The effect of annealing on the XRD patterns of the Ge:Mn films is shown in Fig. 2. Data for the singly implanted films is shown. The annealing dependence of the XRD patterns of the multiply implanted films was identical. Observe that the SI_C200 film remains amorphous through the long anneal at 200°C, while the SI_C330 and SI_FLA films are polycrystalline. In contrast to the SPE annealing of aGe_C330, it appears the presence of Mn hinders the SPE process in SI_C330. There are no extra peaks corresponding to Mn_5Ge_3, $Mn_{11}Ge_8$ or GeO_2 in the XRD patterns of any sample.

The Mn profiles obtained by SRIM software[19] are in very good agreement with the SIMS profile of the as-implanted samples shown in Fig. 3. The singly implanted sample (SI_NA) displays a skewed Gaussian distribution of Mn with peak concentration of roughly 0.34 % near 2.5 μm. The average Mn concentration in SI_NA is about 0.23 % calculated for the effectively implanted (1-3μm) region. Employing multiple implantation process results in a wider Mn distribution (0-3 μm) with average concentration of about 0.08 %. The average Mn concentration is below the maximum solubility (0.7-0.9%) noted above[10].

The effects of both conventional annealing and FLA upon the initial manganese distribution are shown in Fig. 3. Assuming no desorption of Mn from the surface, the

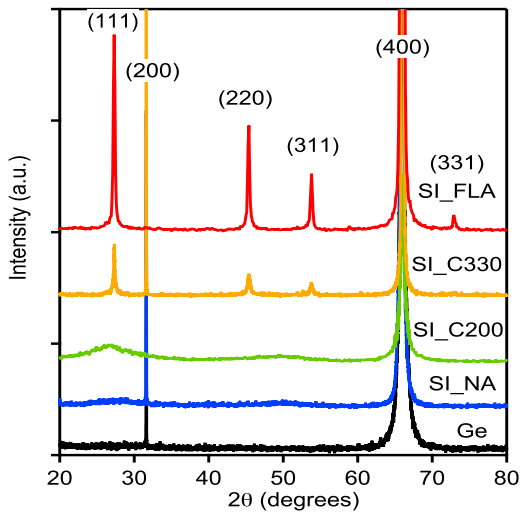

FIG. 2. (Colour Online) XRD patterns of singly implanted samples before (SI_NA) and after conventional annealing at 200° C (SI_C200), 330° C (SI_C330) and flash lamp annealing (SI_FLA)

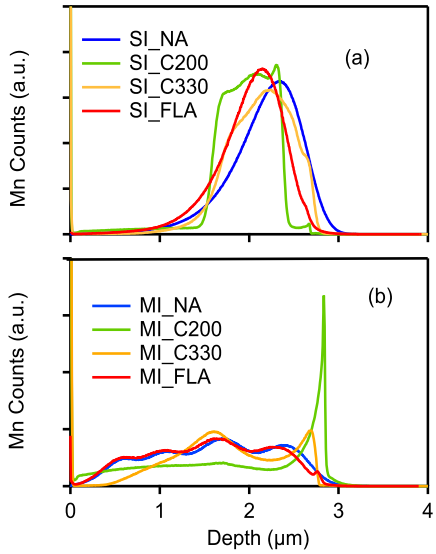

FIG. 3. (Colour Online) Top: SIMS Mn profile in Ge for singly implanted sample before (SI_NA) and after various annealing process (SI_C200, SI_C330, SI_FLA). Bottom: SIMS Mn profile in Ge for multiply implanted sample before (MI_NA) and after various annealing process (MI_C200, MI_C330, MI_FLA).

SIMS profiles shown in Fig. 3 have been normalized to the as-implanted Mn profile curves. This is reasonable as Mn desorption is observed[10] only for T> 600°C. While all three annealing processes produce some movement of Mn ions, the results are in stark contrast to similar work performed in InP:Mn films[12] in which rapid thermal annealing produces SPE of the amorphous layers and sweeps most manganese towards the surface[12]. In contrast, the Mn stays distributed throughout the original 3 μm implantation layer. The magnetic data, to be discussed below show that annealing fosters clustering of Mn into

Mn_5Ge_3 and other Mn-rich regions.

Consider the difference between the SIMS profiles of the singly implanted samples in Fig. 3(a). Note that the greatest movement of Mn occurs in the sample annealed at the lowest temperature (SI_C200). A number of factors might contribute to this. Firstly, isolated Mn ions should diffuse more freely in the amorphous matrix of SI_C200 despite the lower annealing temperature than in SI_C330 and SI_FLA which recrystallize. Secondly, ab-initio electronic structure calculations[20] have shown that clustering reduces the energetic cost of forming interstitial impurities permitting a second diffusion channel in addition to the vacancy mediated diffusion of isolated Mn ions in crystalline Ge[10]. This could provide a kind of positive feedback making the diffusion coefficient of Mn both space- and time-dependent as clustering would produce more effective Mn diffusion inside and around extant clusters. Finally, the longer annealing time in SI_C200 provides the largest total thermal budget for Mn clustering. In support of these suggestions, the magnetic data, to be discussed below, indicate that the lowest fraction of implanted Mn ions remaining isolated and not in clusters is found in sample SI_C200.

There are also interesting differences between the SIMS data of the singly and multiply implanted samples in the end-of-range region. Note that in all of the singly implanted samples, Mn moves away from the c/a interface. On the other hand, in samples MI_C200 and MI_C330, there appears to be movement of Mn towards the c/a interface. This is possibly because the difference in total fluence produces different initial conditions in the microstructure of the end-of-range region and - as was suggested above - this would produce a different evolution in time and space of the effective Mn diffusion rate. The data suggest that the initial Mn diffusion rate in the end-of-range region is larger in the multiply implanted samples than in the singly implanted samples. It has been shown experimentally[21] that low temperature annealing introduces additional extended interstitial defects in the end-of-range region which could increase Mn diffusion and that the number and size of these extended defects is not conserved and decreases with higher temperature annealing. The difference in Mn concentration profile between samples SI_200 and MI_C200 requires further study.

IV. MAGNETIC CHARACTERIZATION

The magnetic characterization was done using a Quantum Design vibrating sample SQUID magnetometer (MPMS-VSM). The zero field cooled (ZFC) magnetization was measured by raising the sample temperature to above room temperature and then cooling the sample down to 5K under zero magnetic field followed by measuring the magnetization in a 100 G field while warming up. The FC magnetization was recorded following the ZFC measurement during cooling down in a 100 G field. Field dependent magnetization was measured at several different temperatures for selected samples.

The magnetic data of the Ge:Mn films before and after annealing are shown in Figs. 4, 5 and 6. To facilitate intersample comparison, all of the data in these figures has been adjusted to be the response of a 50 mg implanted substrate. Hence Figs. 4, 5 and 6 show the response of 2.89×10^{15} Mn ions in multiply implanted thick films and 5.78×10^{15} Mn ions in singly implanted films. The moments are plotted rather than magnetization since, as will be seen below, the samples are inhomogeneous after annealing. Panels (b) and (d) of Figs. 4, 5 and 6 show the FC/ZFC response, while panels (a) and (c) show the magnetic moment versus applied field at T=5K, after removal of the diamagnetic response of the substrate. Observe that the magnetic moments of the singly implanted samples are roughly twice as big as the multiply implanted samples as expected.

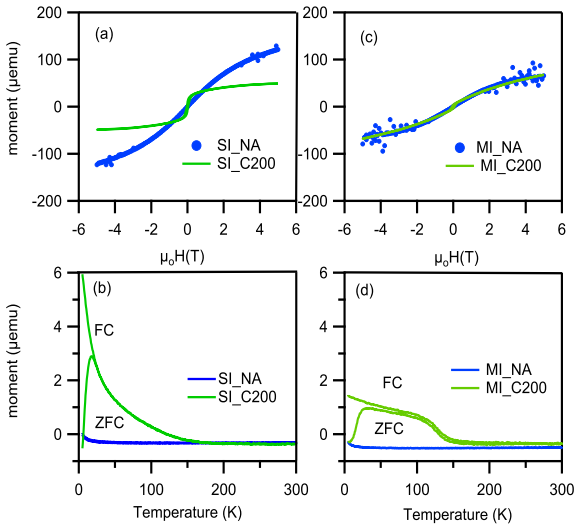

FIG. 4. (Colour Online) Panels (a),(c): Moment versus applied field measurements performed at T=5K before and after 200°C annealing. Panels (b),(d): Zero-field-cooled (ZFC) and field-cooled (FC) magnetic moment versus temperature under applied magnetic field of 100 G before and after 200°C annealing. Data shows the response of 2.89×10^{15} Mn ions in multiply implanted thick films and 5.78×10^{15} Mn ions in singly implanted films. See text for details.

Examination of Figs. 4,5 and 6 reveals several changes produced by annealing. Concerning the MH response, note that the high field moment of the samples decreases after annealing (with one exception, MI_C200). Secondly, the high field M-H response (T=5K) does not saturate for any of the samples.

Turning to the ZFC/FC response observe that annealing causes the ZFC and FC responses to be different which is evidence of Mn clustering. Note that the temperature at which ZFC is maximum depends on the type of annealing. For example, the maximum ZFC response is near T=17K or 25K in SI_C200 and MI_C200, respectively (Fig.4(b) and (d)) and near 130 K for both samples MI_C330 and SI_C330 (Fig. 5(b) and (d)). The ZFC/FC response of samples MI_FLA and SI_FLA is more complicated. Note that two local maxima, one below 30 K and one near room temperature can be seen in sample MI_FLA in Fig. 6.

Three previous works are especially significant in the

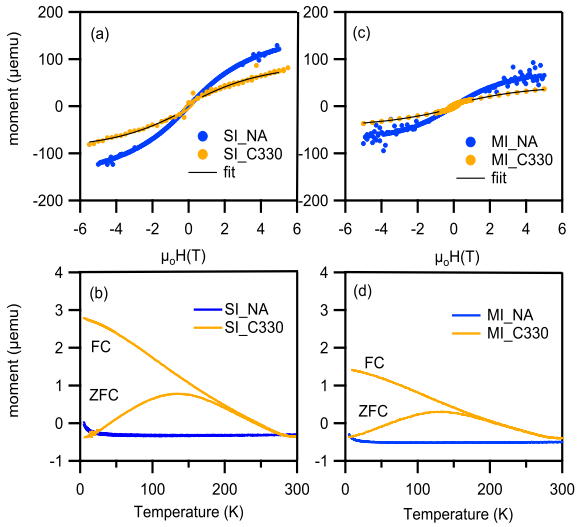

FIG. 5. (Colour Online)Panels (a),(c): Moment versus applied field measurements performed at T=5K before and after 330°C annealing. Panels (b),(d): Zero-field-cooled (ZFC) and field-cooled (FC) magnetic moment versus temperature under applied magnetic field of 100 G before and after 330°C annealing. Data shows the response of 2.89×10^{15} Mn ions in multiply implanted thick films and 5.78×10^{15} Mn ions in singly implanted films. The black curves are fits to the model response consisting of a mixture of dispersed Mn ions and Mn-rich or Mn_5Ge_3 nanoparticles. See text for details.

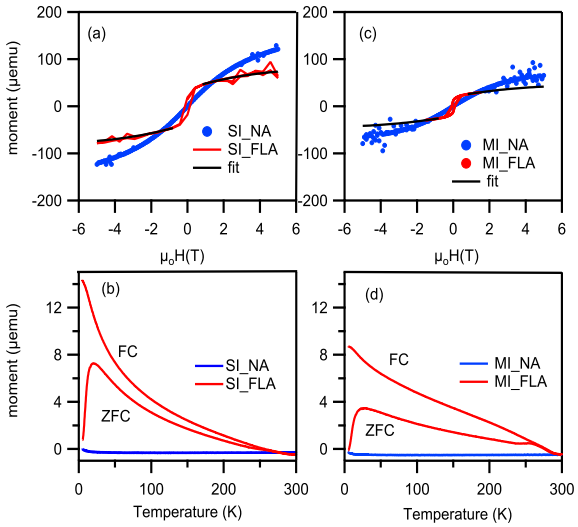

FIG. 6. (Colour Online) Panels (a),(c): Moment versus applied field measurements performed at T=5K before and after flash lamp annealing. Panels (b),(d): Zero-field-cooled (ZFC) and field-cooled (FC) magnetic moment versus temperature under applied magnetic field of 100 G before and after flash lamp annealing. Data shows the response of 2.89×10^{15} Mn ions in multiply implanted thick films and 5.78×10^{15} Mn ions in singly implanted films. The black curves are fits to the model response consisting of a mixture of dispersed Mn ions and Mn-rich or Mn_5Ge_3 nanoparticles. See text for details.

interpretation of the present magnetic data. The first is a study of Ge:Mn films fabricated by low-temperature molecular beam epitaxy (MBE) whose ZFC/FC response is quite similar to that observed in Fig. 4(b) and in which the maximum ZFC response is near 18 K[3]. In these films, Mn-rich clusters of diameter 3-4 nm were observed using transmission electron microscopy (TEM). Bougeard et al. were able to model the M-H response of the Mn-rich nanoclusters using the Langevin model and an average cluster moment of 435 μ_B between 60 K and 160K where the Brillouin response of any remaining isolated Mn ions would be very small and could be neglected. The second work that is helpful for our interpretation concerns Ge:Mn thin layers ($t \approx 100$ nm) prepared by implantation of 100-keV Mn ions into nearly intrinsic Ge substrates held at 300° C (673 K) to avoid amorphization[22]. These films contained Mn_5Ge_3 nanoparticles identified by XRD and TEM. By varying the implantation fluence the average Mn concentration and Mn_5Ge_3 nanoparticle size could be controlled. It is significant that the ZFC/FC response of these inhomogeneous films was quite similar to that observed in Fig. 5 and that the temperature of the ZFC maximum could be correlated with average Mn_5Ge_3 nanoparticle size. The third work that is significant for the interpretation of the magnetic data is a systematic study of the size dependence of the magnetic properties of Mn_5Ge_3 nanoparticles in which three trends were observed: the temperature of the maximum ZFC reponse, the moment per Mn ion and the coercive field all increase with particle size[23]. A summary of the data from these three papers appears in Tables II and III. It is curious that the magnetic properties of the free Mn_5Ge_3 nanoparticles[23] are similar but not identical to the nanoparticles existing in the Ge:Mn films[22].

One can compare the magnetic properties of the present Ge:Mn thick films with the aforementioned studies in Tables II and III. It can be argued that the different annealing processes employed in this work produce two different kinds of inclusions: Mn-rich nanoclusters, which contain $\approx 10-15\%$ Mn, and Mn_5Ge_3 nanoparticles. Based on similarities of the ZFC maxima and coercive field, the data in Tables II and III suggest that conventional annealing at 200°C produces Mn-rich nanoclusters of small radius ($\approx 3-4$ nm) while conventional annealing at 330°C produces larger Mn_5Ge_3 inclusions ($\approx 7-10$ nm). The flash lamp annealed samples contain both kinds of inclusions where the Mn_5Ge_3 inclusions are larger in the flash lamp annealed samples ($\approx 11-12$ nm) than in the conventionally annealed samples. Also listed in Tables II and III are the moments of the Mn that has migrated to the clusters which are lower than the moments of the dispersed Mn atoms (3-3.4μ_B) and were obtained from the model to be discussed below.

A key to separating the different response of the dispersed and clustered Mn appears in Fig. 7, which illustrates the MH response of a singly implanted Ge:Mn thick film before and after conventional annealing at 200°C. Before annealing, the response can be modeled using the Brillouin function for non-interacting moments where the Mn moment is between 3 and 3.4 μ_B. After annealing, note that complete saturation is achieved at T=100K, but that at T=5K, the moment is continuing to increase even at $\mu_o H = 5$T. This is because of the much

TABLE II. Mn-rich nanocluster data ($\approx 10-15\%$ Mn) taken from reference 3 compared with data for relevant Ge:Mn samples believed to contain the nanoclusters. H_c is the coercive field.

average radius (nm)	T_{max} ZFC (K)	$\mu_o H_c$ (Tesla)	μ_B per Mn (clusters)	reference
3-4	18	0.045 (6.5K)	0.25-1	Ref. 3
sample				
SI_C200	17.5±1	.04±.005 (5K)	0.62±.02	
MI_FLA	26±3	NA	NA	
SI_FLA	20.5±1	NA	NA	

TABLE III. Mn_5Ge_3 nanoparticle data taken from references 22 and 23 compared with data for relevant Ge:Mn samples believed to contain the nanoparticles. H_c is the coercive field.

average radius (nm)	T_{max} ZFC (K)	$\mu_o H_c$ (Tesla)	μ_B per Mn (nanoparticles)	reference
5	185	0.22 (5K)	1.1	Ref. 22
7.2±0.9	125	0.04 (50K)	0.075	Ref. 23
10±1.6	175	0.05 (50K)	0.11	Ref. 23
11	270	0.26 (5K)	1.5	Ref. 22
12±3	260	0.13 (50K)	0.42	Ref. 23
sample				
MI_C330	130±5	0.15±.01 (5K)	0.29±.04	
SI_C330	133±3	0.15±.01 (5K)	0.20±.02	
MI_FLA	253±2	NA	NA	
SI_FLA	260±5	NA	NA	

greater contribution of the dispersed Mn at T=5K than at 100K. These observations can be modelled assuming that a fraction of the implanted Mn remains dispersed and follows the Brillouin function while the remainder contributes a constant at high field (between 3 and 5T).

$$\mu_{TOT} = N_f g J \mu_B B_J(\frac{gJ\mu_B B}{kT}) + (N - N_f) * \mu_C \quad (1)$$

In Eq. 1, N is the total number implanted Mn which is fixed by the implantation and N_f is the number of dispersed Mn. It is assumed that moment of dispersed Mn is fixed between $3-3.4\mu_B$ per Mn, which gives the best fit to the non-annealed samples and is close to value expected for substitutional Mn[1,24]. The dispersed Mn moment is larger than the moment of Mn in the clusters (μ_C). N_f and μ_C are the fitting parameters.

Note that the Langevin function[3] used by Bougeard et al. to model the response of the superparamagnetic Mn-rich clusters saturates below $\mu_o H$ =1.0T . In Eq. 1, which applies only at high field, it is assumed that annealing does not alter the moment of the dispersed Mn ($gJ\mu_B$), but the moment of the Mn in clusters (μ_C) is a free parameter which turns out to be less than the fixed dispersed moment. This does not yet have an explanation but is in agreement with the observations of three previous groups as seen in Tables II and III.

At T=5K, the slope and curvature at high field in the M versus H measurement are sensitive to the fraction of Mn behaving as isolated spins, while the constant contribution determined in the fit allows one to determine the average Mn moment in the clusters. For fitting the annealed samples the moment of the free Mn ions was fixed between 3 or $3.4\mu_B$ consistent with the moment of the non-annealed samples. At T=100K, we assume a mixture of the Brillouin and Langevin functions for the dispersed and clustered Mn, respectively, where the only remaining free parameter is the average nanocluster moment (550 μ_B) which is determined by the slope of the M-H curve near H$\approx$ 0. Note that the cluster moment determined for SI_C200 is about the same as that found[3] for the manganese rich clusters (435 μ_B) in Ge:Mn produced by low temperature MBE. In the two theoretical curves for SI_C200 shown in Fig. 7, only the temperature changes. The agreement between the data and the model is very good.

Using the same model, fits to the C330 and FLA samples were made and are shown in Figs. 5 and 6 where the fitting parameters are shown in Table IV. The uncertainties in the fit parameters result from uncertainty in the assumed moment of the dispersed Mn (between 3 and 3.4 μ_B). That is, we fix dispersed moment for the fit and get different final fitting parameters depending on the assumed dispersed moment. The volume fractions listed in Table IV for the samples annealed at 330°C assuming only Mn_5Ge_3 inclusions are calculated by dividing N_f by 10 to determine the number of unit cells of Mn_5Ge_3 and then dividing the total volume of Mn_5Ge_3 by the film volume. For sample SI_C200, which contains Mn-rich clusters in lieu of Mn_5Ge_3, this number is multiplied by 6 since the Mn-rich clusters contain only 10% Mn. The uncertainty in f for the FLA samples is much larger since the contributions of Mn-rich nanoclusters and Mn_5Ge_3 nanoparticles cannot be separated.

Note that MI_C200 is excluded from both the analysis and the table since its ZFC/FC response is more complicated than the others (there is evidence of transitions near 25K, 150K and 250 K) and the MH response does not show the marked decrease in Mn moment upon annealing that all the other samples do.

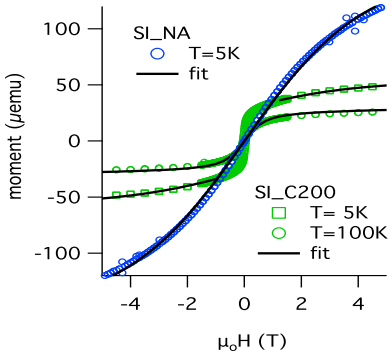

FIG. 7. (Colour Online) Magnetic moment versus applied field of single implanted Ge:Mn before (SI_NA, T=5K) and after annealing (SI_C200, T=5K and T=100K). The theoretical curve for SI_NA is a Brillouin function, while the theoretical curves for SI_C200 are either Eq. 1 (T=5K) or, at T=100K, a mixture of the Brillouin function (isolated Mn ions) and Langevin function (Mn rich nanoclusters) with parameters listed in Table IV.

TABLE IV. Free and Clustered Mn data obtained from fits of the high field M-H data to Eq, 1. The fitting parameters are N_f, from which the % Mn dispersed is obtained, and μ_C which is the average Mn moment in the Mn_5Ge_3 nanoparticles or Mn-rich clusters containing approximately 10% Mn. As argued in the text, the FLA samples contain both of these entities which is the reason for the larger uncertainty in f for these samples.

Sample	% Mn dispersed (N_f/N ×100%)	average dispersed Mn density ($\times 10^{19}$cm^{-3})	average Mn moment Mn_5Ge_3 or Mn-rich clusters (μ_C in μ_B)	vol. frac. Mn_5Ge_3 or Mn-rich clusters (f)
MI_NA	100	3.3	-	-
MI_C330	46±3	1.5 ± 0.1	0.29±.04	.0004-.00041
MI_FLA	30±3	1.0 ± 0.1	1.12±.04	.0005-.0032
SI_NA	100	6.6	-	-
SI_C200	18 ±1	1.2 ± 0.1	0.62±.02	.0073-.0075
SI_C330	49±4	3.3 ± 0.3	0.20±.02	.00075-.00078
SI_FLA	26±2	1.7 ± 0.2	0.96±.04	.0011-.0067

V. INFRARED CHARACTERIZATION

A. Experimental Details and Data Analysis

The infrared transmission was measured using a Bruker /66V IFS fourier transform interferometer with samples mounted on a Janis continuous flow cryostat with sample position and reference controlled by a McAllister BLT Linear translator. The data were collected at normal incidence at 4 cm^{-1} resolution which was low enough to suppress Fabry-Perot fringes due to internal reflections from the surfaces of the substrate.

The optical response functions of the implanted layers were extracted by fitting the transmission data to a two-layer model using RefFIT software[25]. Although the implanted layers in all the annealed samples are inhomogeneous, they are modeled as having a single effective dielectric function. The model for the dielectric function of each layer implements minimal Lorentz oscillators to capture the main features of the spectrum and avoid overfitting.

The first step was to determine the dielectric function of the substrate, by simultaneously fitting three sets of data: the transmission data measured in this work, refractive index data[26] and reflectance data[27]. Then, by fixing the substrate dielectric function, the effective dielectric function of the Ge:Mn layers could be extracted by fitting the measured transmission of the two layer system. The thickness of the implanted layer was sometimes a fitting parameter as will be discussed below. The effective dielectric function of the implanted layers was constructed as a sum of Lorentz oscillators with one Drude oscillator if free carrier behaviour was involved.

B. Intrinsic Ge Absorption

The room temperature transmission of the substrate appears in the top panel of Fig. 8 in which two regions of strong absorption can be observed: the far-infrared 50-500 cm^{-1} region where two-phonon absorption[28,29] takes place and the onset of interband absorption above 5000 cm^{-1}. The dielectric function of high resistivity substrates included the following contributions:

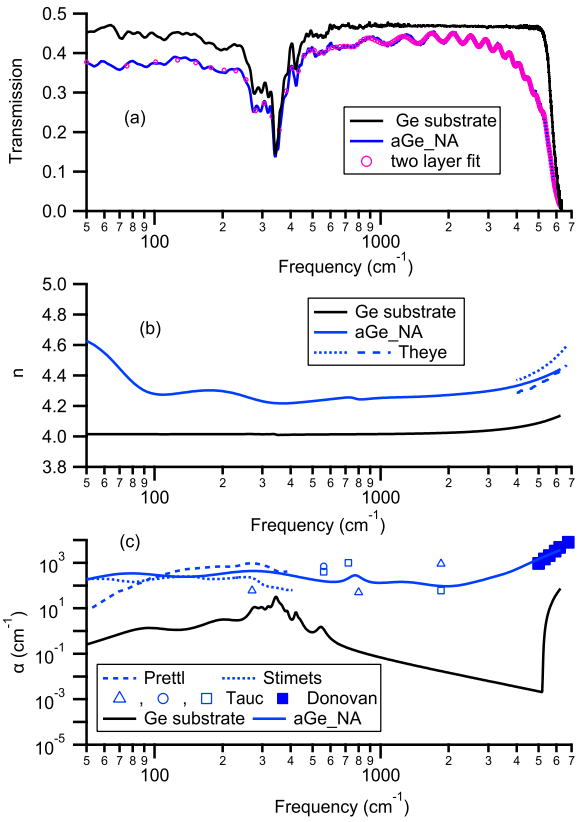

FIG. 8. (Colour Online) Top: Transmission versus frequency (T=300 K) for Ge substrate and self-implanted sample aGe_NA. Also shown is the two-layer fit determined using RefFIT. Middle: Index of refraction determined using RefFIT of the substrate and sample aGe_NA as well as literature data (Theye[30]) for amorphous Ge. Bottom: absorption coefficient of substrate and sample aGe_NA determined using RefFIT as well as literature data for amorphous Ge prepared by a variety of techniques (Prettl[31], Stimets[32], Tauc[33], Donovan[34]).

$$\epsilon = \epsilon_\infty + \epsilon_{TL} + \sum_i \epsilon^i_{Lor} \qquad (2)$$

The band gap absorption was fit to a Tauc-Lorentz dielectric function (ϵ_{TL}). ϵ_{TL} originally was developed to account for the modified absorption edge in amorphous materials[35,36] but can be also used to describe the band gap absorption in crystalline materials[37]. Combining the Tauc joint density of states[38] with a Lorentzian absorption the Tauc-Lorentz formula for the imaginary part of

the dielectric function is given by[35,36].

$$\epsilon_{2TL}(\omega) = \begin{cases} \frac{A\omega_0 C(\omega-\omega_g)^2}{(\omega^2-\omega_0{}^2)^2+C^2\omega^2}\frac{1}{\omega} & \omega > \omega_g \\ 0 & \omega \le \omega_g \end{cases} \quad (3)$$

where E_g is the optical band gap, E_0 is the peak energy and C is the broadening of the peak. A reflects the amplitude of ϵ_2 peak while ϵ_{1TL} is determined from ϵ_{2TL} by the Kramers Kronig transform[35,36].

The two phonon absorption in crystalline Ge in the FIR range of the spectrum (100-600 cm^{-1}) was fit to a sum of Lorentzian terms where each Lorentzian is characterized by three parameters: strength (ω_p), center frequency (ω_o), and width (γ).

$$\epsilon_{Lor} = \frac{\omega_p^2}{\omega_0^2 - \omega^2 - i\gamma\omega} \quad (4)$$

The frequencies of the phonons obtained from the fits are in good agreement with previously determined values[28]. Table V lists the final fitting parameters for the model dielectric function of the intrinsic properties of high resistivity Ge substrate. The uncertainty values indicate the range of final fitting parameters found after beginning the fit with different sets of starting parameters.

The bottom panel of Fig. 8 presents the absorption coefficient $\alpha(\omega)$ for the high resistivity substrate derived from the dielectric function of Eq. 2 using the parameters from Table V. While not shown, the agreement with previous measurements in the two phonon absorption region[28,29] and band gap region[39] is excellent.

TABLE V. Fitting parameters obtained from RefFit for intrinsic Ge properties (thickness = 325μm) at room temperature. ϵ_∞=8.8±0.1. All table entries in cm^{-1}. If uncertainty is not listed it is less than ±0.1

ϵ_{TL}	ω_0	ω_g	A	C
	18760 ±50	5248 ±1	2.72±0.03 × 10^5	1018±5
ϵ^i_{LOR}	ω_0	ω_p	γ	
	103 ± 5	5± 1	28 ± 15	
	196 ± 2	11.5 ± 0.3	73 ± 3	
	276.7	13.6	31.4 ±0.2	
	295 ± 5	8.3	18.6 ± 0.1	
	318	7.2	12.9	
	344.2	19	19	
	364	10.6	22.7	
	386	5.2	11.1	
	421.4 ± 0.2	6.1	12.5	
	435	5.6	24.9	
	520 ± 17	9.7	77.9 ± 0.6	

C. Amorphous Germanium

Also shown in the upper panel of Fig. 8 is the 300 K transmission spectrum of sample aGe_NA compared with the final fit determined by RefFIT. The three main effects of the amorphization of the implanted Germanium layer are the lowering of transmission across the spectrum, the broadening of the interband absorption feature between 4000 and 6000 cm^{-1}, and the introduction of interference fringes between 1000-6000 cm^{-1}.

The dielectric function of the amorphous layer was also modeled using Eq. 2, however the Lorentzians do not represent absorption by the two-phonon process. Instead they account for extra absorption processes induced by amorphization which produce the decrease in the transmitted intensity across the whole spectrum. The fitting parameters determined by RefFIT appear in Table VI where the uncertainty reflects the range of fitting parameters found by starting the fit at slightly different places in fitting parameter space. One-phonon absorption is permitted in amorphous Ge, and the center frequencies of the lowest frequency oscillators were fixed (indicated by uncertainty ±0 in Table VI) to previously observed maxima in the phonon density of states[40]. The fringe spacing in the transmission spectra is determined primarily by the thickness of the amorphous layers. TEM imaging (not shown) of the as-implanted SI_NA sample, revealed a remnant of crystalline order near the end of implanted ion range. Since the degree of crystallinity is changing over a range of depths we can only define an effective thickness which is then a fitting parameter.

TABLE VI. Fitting parameters obtained from RefFit for self-implanted aGe-NA at room temperature. Layer thickness is 2.79 ± .05μm, ϵ_∞=8.3±0.1. All table entries in cm^{-1}.

ϵ_{TL}	ω_0	ω_g	A	C
	18500±300	2750±60	2.68±.03×10^5	3960±100
ϵ^i_{LOR}	ω_0	ω_p	γ	
	75± 0	123± 5	70 ± 6	
	275 ± 0	290 ± 20	300± 30	
	768 ± 3	123 ± 3	129 ±2	
	1263 ± 6	260 ± 20	900± 20	
	3200 ± 100	490 ± 50	1900 ± 200	

The optical response functions of amorphous Germanium are highly sensitive to preparation conditions[30–34,38,40]. Literature values for n and α of amorphous Ge prepared by a variety of techniques can be seen in Fig. 8 to compare with the values determined for amorphous Ge prepared in this work (sample aGe_NA).

D. Ge:Mn Thick Films

The implantation and annealing dependence of the infrared transmission at room temperature is shown in Fig. 9. The transmission of samples MI_NA and SI_NA is quite similar to that of the amorphous Ge film, aGe_NA discussed above. Conventional annealing at 200°C produces only minor changes in the transmission spectra in both singly and multiply implanted films. On the other hand, both FLA and conventional annealing at 330°C produce significant changes that will be discussed below. The minor changes produced by conventional annealing at 200°C to the index of refraction and absorption coefficient of sample SI_NA can be seen in Fig. 10, where the optical response functions have been extracted using the two-layer model discussed above. The data for only

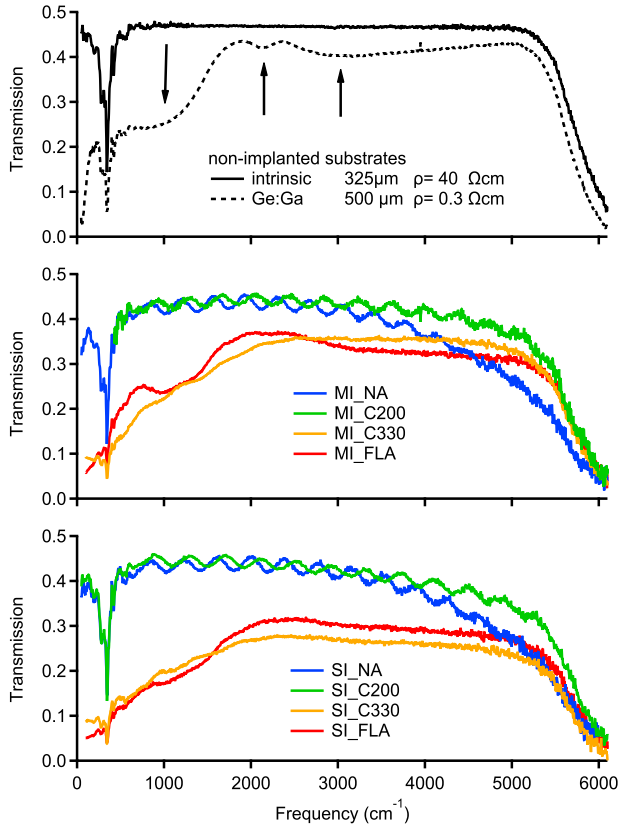

FIG. 9. (Colour Online) Top: Transmission versus frequency (T=300 K) for high resistivity Ge substrate and low resistivity p-type Ge substrate. Middle: Annealing dependence of transmission versus frequency (T=300 K) of multiply implanted samples. Bottom: Annealing dependence of transmission versus frequency (T=300 K) of singly implanted samples.

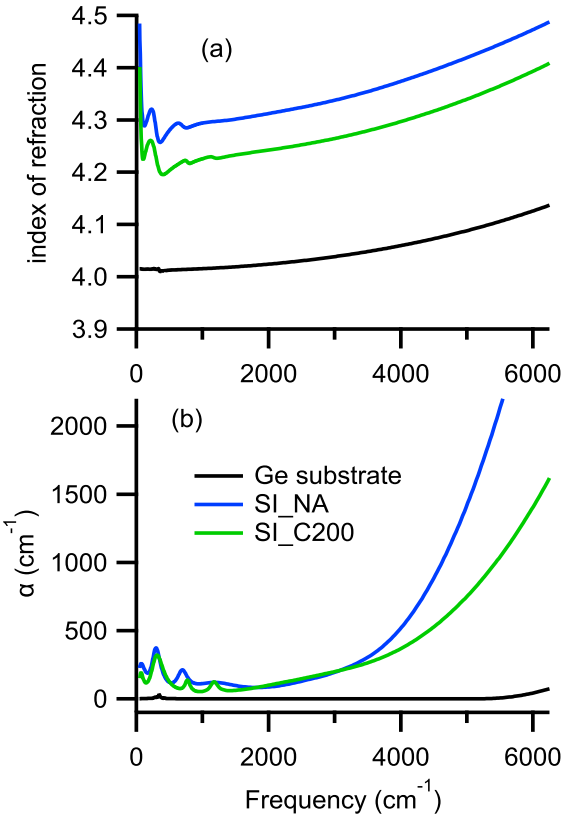

FIG. 10. (Colour Online) Top: refractive index versus frequency (T=300 K) for SI_NA and SI_C200 and the Ge substrate. Bottom: absorption coefficient versus frequency for SI_NA and SI_C200 and the Ge substrate.

SI_NA and SI_C200 are shown because the response functions of the multiply implanted samples are similar. Note that conventional annealing at 200°C has two main effects: a slight movement in the values of n and α towards the values of the Ge substrate which is expected as the film begins to recrystallize. This accounts for the slight increase in fringe spacing and increase in transmission near the onset of interband absorption.

Comparison of the absorption coefficients of Figs. 8 and 10 should, in principle, reveal Mn-specific absorption. Photoconductivity data[41,42] indicate that in crystalline Ge:Mn, Mn is a double acceptor with deep levels 1290 cm^{-1} (0.16 eV) above the valence band (VB) and 2980 cm^{-1} (0.37 eV) below the conduction band (CB) at 77 K. However, the same four absorption features for $\omega < 2000$ cm^{-1} listed in Table VI appear in both amorphous Ge:Mn and self-implanted films. There are no new spectral features in the absorption coefficients of SI_NA and SI_C200 in Fig. 10 that can be associated with these previously observed Mn impurity levels. Observe, on the other hand, the significant changes produced by annealing in the transmission spectra of the C330 and FLA samples in Fig. 9: the depression of the transmission below 2000 cm^{-1} which suggests absorption by free carriers as well as the frequency dependent features similar to the p-type Ge:Ga substrate shown in the upper panel, especially in sample MI_FLA.

Since Mn is a double acceptor, it is crucial to understand the infrared transmission spectrum of p-type Germanium, an example of which (the Ge:Ga substrate with $p = 1.5 \times 10^{16}$ cm^{-3}) is shown in the top panel of Fig. 9. In comparison with the transmission spectrum of high resistivity Ge, there are four additional features in the spectrum of p-type Ge: the Drude absorption which is responsible for the low transmission below 500 cm^{-1} and three inter-valence band transitions indicated by the arrows. These are between the light-hole and the heavy-hole band (1000 cm^{-1}), between the split-off band and the heavy hole band (3200 cm^{-1}) and between the split-off band and the light hole band (2400 cm^{-1})[43]. It has been previously observed that the strength of these three transitions scales with the hole density and the frequency dependence of the absorption coefficient between 1000 and 5000 cm^{-1} is somewhat independent of the type of dopant atom[44,45].

Further complicating the interpretation of the transmission spectra is the fact that the combined XRD and magnetic data suggest that the Ge:Mn thick films are mixtures of metallic Mn_5Ge_3 nanoparticles and semiconducting Ge:Mn grains. Consider previous work on composites of small silver particles and KCl grains[46]: The infrared response of the composite is that of an insulator if the volume fraction of silver is less about 30%, and that of a metal if greater than about 30%. In other words,

the effective optical response function of the composites displayed the percolation transition. As seen in Table IV the present Ge:Mn films are far from the percolation transition since the estimated metallic volume fractions are less than 0.1%. Both the Maxwell-Garnett model and the Bruggeman model give the same result for the effective dielectric function for a composite with a small volume fraction minority phase[46,47].

The effect of Mn_5Ge_3 inclusions was explored using the Bruggeman model where the dependence of effective medium dielectric function ϵ^*, on the metal inclusion (ϵ_M - fraction f) and background (ϵ_B) dielectric functions is given by[48]:

$$\epsilon^* = \frac{1}{4}\left[\gamma + \sqrt{\gamma^2 + 8\epsilon_M\epsilon_B}\right] \quad (5)$$

where

$$\gamma = (3f-1)\epsilon_M + (2-3f)\epsilon_B \quad (6)$$

Taking, as ϵ_B, the dielectric function of pure Ge discussed above with parameters listed in Table V and, as ϵ_M, the dielectric function of Mn_5Ge_3 (see Table VII), the effective medium absorption coefficient is plotted as a function of f in Fig. 11. It is interesting to note that for the small volume fractions (see Table IV) expected for the present Ge:Mn thick films, the main effect of the metallic inclusions is to raise the conductivity by a small amount in the region of between the two-phonon absorption and the onset of interband transitions. The expected absorption resonance for metallic particles in semiconducting substrates is not resolvable inside the band gap of Ge in contrast to observed resonance of MnAs inclusions in GaAs:Mn[49]. The Bruggeman theory results shown in Fig. 11, help one to understand the frequency dependence of absorption coefficient for the metallic Ge:Mn thick films. It will be seen that the absorption coefficient of the films is dominated by the background dielectric function which is provided by the Ge matrix containing isolated Mn acceptors and free holes. The absorption spectra of the metallic Ge:Mn films were extracted using the two-layer model and variational dielectric fitting[25] and are shown in Fig. 12. For comparison, the absorption spectrum for a p-type Ge:Ga substrate is also shown in the bottom panel of the figure. In this bottom panel, notice the free-hole related features (a Drude peak prominent for $\omega < 200$ cm^{-1} and the three inter-valence-band absorption bands at 1000, 2400 and 3200 cm^{-1}) in addition to the band gap feature near 5000 cm^{-1} and the two phonon absorption peaks between 100 and 600 cm^{-1}. As stated earlier, the strength of the inter-valence-band absorption scales with the free hole density, and so included in the bottom panel are the absorption coefficients of p-type Ge containing shallow acceptors (Ge:In) and deep acceptors (Ge:Au) scaled for a hole density $p = 1.5 \times 10^{16}$ cm^{-3}. Note the somewhat better agreement of the measured absorption coefficient with that predicted from Ge:In[44] rather than Ge:Au[45], which makes sense since Ga is a shallow acceptor. The extra absorption between 3000 and 5000 cm^{-1} in Ge:Au may be due to transitions from the Au-acceptor levels to the conduction band. The parameters used to fit the Drude peak shown in the bottom panel of Fig. 12 are listed in Table VIII and are close to the values obtained from electrical transport data for Ge:Ga assuming single band (heavy-hole) conduction (i.e. $\omega_p = 69$ cm^{-1} and $\Gamma = 21$ cm^{-1})[51]. There are two possible models for where the holes produced by Mn-doping reside. They could be moving in either the VB of the parent material or they could be moving in an impurity band. The IR data, at least for sample MI_FLA seem to support the former interpretation. Consider the absorption coefficient of the MI_FLA sample shown in the middle panel of Fig. 12 which differs from the parent substrate simply by the addition of approximately 3×10^{18} cm^{-3} of free p-type carriers; the presence of a small volume fraction of Mn_5Ge_3 does not significantly contribute to the mid-infrared absorption. This statement can be supported by comparing the measured absorption coefficient of MI_FLA with the free carrier response which consists of two pieces: the Drude response and the inter-valence-band transitions.

TABLE VII. Drude-Lorentz Model fitting parameters (Eq. 4) for Mn_5Ge_3 assuming $\epsilon_\infty = 1$. The parameters were obtained by fitting the 300K reflectance data of Mn_5Ge_3[50] to a Drude-Lorentz model.

ω_o (cm^{-1})	γ (cm^{-1})	ω_p (cm^{-1})
0	160	9450
1045	6750	33800
13700	21600	36000

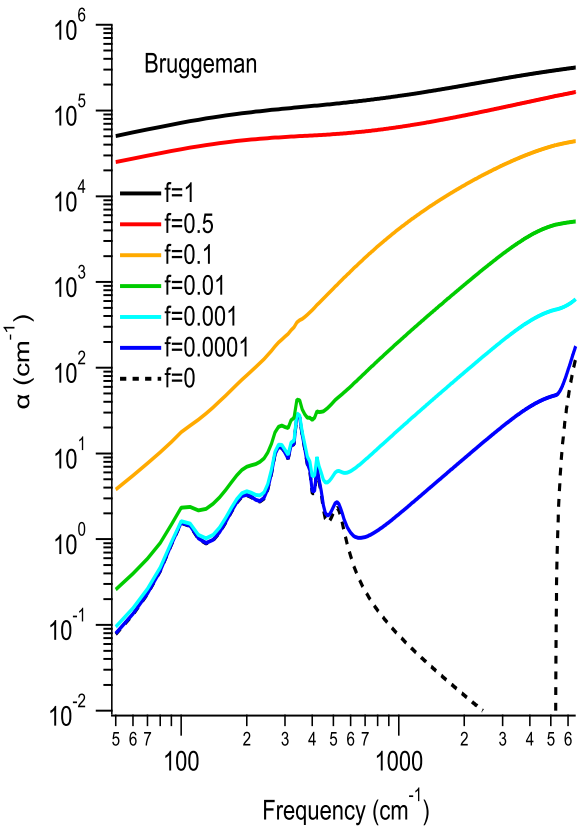

FIG. 11. (Colour Online) Absorption coefficient mixtures of Mn_5Ge_3 and pure Ge as a function of f, the volume fraction of Mn_5Ge_3, as predicted by the Bruggeman model, Eq. 5

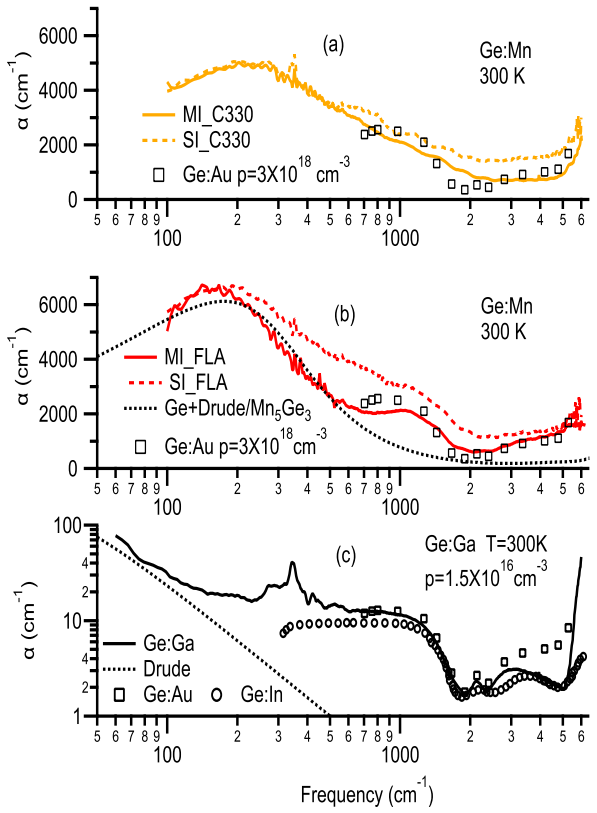

FIG. 12. (Colour Online) Bottom panel: absorption coefficient versus frequency for a Ge:Ga substrate with known hole density 1.5×10^{16}. Also shown are the Drude absorption and the inter-valence band absorption in Ge:In[44] and Ge:Au[45] scaled for hole density p=1.5×10^{16} cm^{-3} Middle: absorption coefficient versus frequency (T=300 K) for MI_FLA and SI_FLA. Also shown is the intervalence band absorption expected for a hole concentration of 3×10^{18} cm^{-3} as well as the prediction of the Bruggeman theory for mixtures of Mn_5Ge_3 ($f = 0.0046$) with the dielectric function of Ge to which a Drude term has been added. Top: absorption coefficient versus frequency (T=300 K) for MI_C330 and SI_C330.

In the middle panel of Fig. 12, the black dashed curve is the absorption coefficient generated by the Bruggeman model (f=0.0005) as discussed above with one difference: a Drude contribution has been added to ϵ_B in addition to the interband and two-phonon contributions of Table V. Note that the Drude contribution cannot account for the whole spectrum of MI_FLA: in addition there is the broad absorption band centered near 1000 cm^{-1} in the spectra of both the MI_FLA and SI_FLA samples. This can be seen to be part of the set of inter-valence-band transitions in p-type Ge by comparing it to the literature data (black squares) of the absorption coefficient of Ge:Au which has been scaled for a carrier density of $p = 3 \times 10^{18}$ cm^{-3}. Traces of this inter-valence-band structure also appear in the absorption spectrum of SI_FLA but the structure is not resolvable of samples MI_C330 and SI_C330 as seen in the upper panel. While perfect agreement is not obtained, we argue that the level of the density of free holes (±50%) can be estimated by matching the level of the inter-valence-band absorption and the measured effective absorption coefficients. These are listed as $p(IVB)$ in Table VIII. Also listed in this table are the Drude parameters for the metallic Ge:Mn samples. An example of the agreement between the model Drude absorption and the absorption coefficient for sample MI_FLA appears in the middle panel of Fig. 12. A second way to estimate the free hole density is to use the Drude plasma frequency and assume single heavy-hole band conduction ($\omega_p^2 = \frac{pe^2}{m^* \epsilon_o}$). These hole density estimates ($p(\omega_p)$) are also listed in Table VIII and are of the same order of magnitude as the hole densities estimated from the level of the inter-valence-band absorption but less than the average non-clustered Mn densities listed in Table IV. This is consistent with the presence of some Mn in interstitial sites which are double donors[20] producing some self-compensation. The excess high frequency absorption above the level of the intervalence band transitions may be due to transitions associated with either interstial Mn levels or, as suggested earlier for Ge:Au, transitions from substitutional Mn levels. The scattering rate (width) of the Drude peak in the Ge:Mn films is much higher than in the Ge:Ga sample as Fig. 12 and Table VIII show. The Drude parameters ω_p, Γ and the carrier density estimated from the level of the inter-valence-band absorption - $p(IVB)$ - can be used to predict the hole mobilities which are also listed in Table VIII. The mobilities are estimated using the following formula assuming single band heavy-hole conduction, where ω_p and Γ are measured in cm^{-1} :

$$\mu_p = \frac{\omega_p^2}{60\Gamma} \frac{1}{p(IVB)e} \tag{7}$$

The uncertainty in μ_p for Ge:Mn comes entirely from the uncertainty in free hole density. It is interesting to compare the estimated mobilities of the Ge:Mn samples with the doping dependence of the mobility in Ge:Ga[52] which can be seen in Fig. 13. Note that the estimated hole mobilities of the Ge:Mn films are roughly an order of magnitude lower than in Ge:Ga. This might be explained by a higher scattering rate due to extra disorder or magnetic scattering in the presence of Mn in both substitutional and interstitial sites but deserves further study.

TABLE VIII. Infrared Fit Parameters. ω_p and Γ are the Drude oscillator parameters. $p(IVB)$ is the hole density estimated from the level of the inter-valence-band absorption coefficient. $p(\omega_p)$ is the carrier density estimated from ω_p assuming $m^* = 0.28$, the heavy hole mass. μ_p is the hole mobility estimated by the Eq. 7.

	ω_p (cm^{-1})	Γ (cm^{-1})	$p(IVB)$ (cm^{-3})	$p(\omega_p)$ (cm^{-3})	μ_p cm^2/Vs
Ge:Ga	71 ± 1	31 ± 1	1.5×10^{16}	1.5×10^{16}	1130
MI_FLA	1240	340	$3 \pm 1.5 \times 10^{18}$	4.8×10^{18}	100
SI_FLA	1520	520	$4 \pm 2 \times 10^{18}$	7.2×10^{18}	65
MI_C330	1440	640	$3 \pm 1.5 \times 10^{18}$	6.5×10^{18}	50
SI_C330	1290	530	$3 \pm 1.5 \times 10^{18}$	5.1×10^{18}	60

TABLE IX. Summary of Sample Properties determined from Magnetic and Infrared Measurements

Sample	Description	% Mn dispersed	volume fraction Mn-rich and/ or Mn_5Ge_3	average dispersed Mn conc. magnetic analysis ($\times 10^{19}$cm^{-3})	average hole concentration IR: $p(IVB)$ ($\times 10^{18}$cm^{-3})	average hole concentration IR: $p(\omega_p)$ ($\times 10^{18}$ cm^{-3})	ratio $p(IVB)$ to dispersed Mn
MI_NA	dispersed Mn	100	0	3.3	0	0	0
SI_NA	dispersed Mn	100	0	6.6	0	0	0
MI_C200	dispersed Mn, Mn-rich clusters	NA	NA	NA	0	0	0
SI_C200	dispersed Mn, Mn-rich clusters	18±1	.0073-.0075	1.2 ± 0.1	0	0	0
MI_C330	dispersed Mn, Mn_5Ge_3	46±3	.0004-.00041	1.5 ± 0.1	3 ± 1.5	6.5	0.2 ± 0.1
SI_C330	dispersed Mn , Mn_5Ge_3	49±4	.00075-.00078	3.3 ± 0.3	3 ± 1.5	5.1	0.10 ± 0.05
MI_FLA	dispersed Mn , Mn_5Ge_3, Mn-rich clusters	30±3	.0005-.0032	1.0 ± 0.1	3 ± 1.5	4.8	0.33 ± 0.16
SI_FLA	dispersed Mn, Mn_5Ge_3, Mn-rich clusters	26±2	.0011-.0067	1.7 ± 0.2	4 ± 2	7.2	0.27 ± 0.13

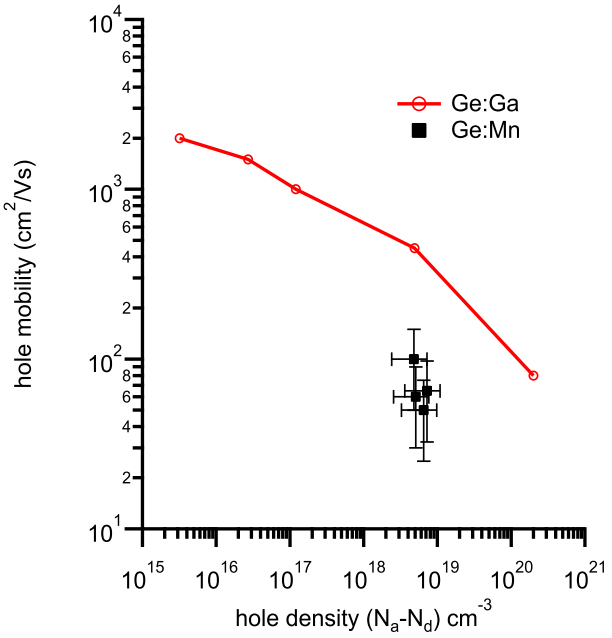

FIG. 13. (Colour Online) Mobility versus hole concentration in Ge:Ga from Ref. 52 and the Ge:Mn thick films.

VI. CONCLUSIONS

Ge:Mn thick films have been prepared by ion-implantation with low average Mn concentration (0.08-0.23%) followed by post-annealing and characterized by a variety of techniques including XRD, SIMS, magnetometry and IR transmission. Table IX presents a summary of the sample properties as extracted from the magnetic and infrared measurements. Briefly, the Mn ions are completely dispersed in the amorphous as-implanted films, while ≈50-80% of Mn atoms migrate to form Mn rich or Mn_5Ge_3 clusters as the films recrystallize upon annealing. Table IX shows that despite the fact that a majority of the implanted Mn moves to the clusters, the volume fraction of these clusters remains far below the percolation transition. The remaining Mn ions enter the Ge lattice and produce holes. In Table IX, note the rough consistency between the density of free holes as determined by the two independent (magnetic, IR) analyses. In addition, it has been seen that the presence of Mn hinders SPE in Ge:Mn. Finally, since clustering is observed after annealing in the samples prepared with the lowest Mn fluence (average Mn concentration ≈ 0.08%) , the data suggest that the maximum equilibrium solid solubility of Mn is an order of magnitude lower than recently suggested.

ACKNOWLEDGMENTS

This research was supported by the National Science and Engineering Research Council of Canada and by the Helmholtz-Gemeinschaft Deutscher Forschungszentren (HGF-VH-NG-713). L. H. Obied would like to thank the Libyan scholarship program in Canada. DC thanks the Helmholtz Forschungszentren- Rossendorf for kind

hospitality.

[1] Y. Park, A. Hanbicki, and T. Jonker, Science **295**, 651 (2002).
[2] A. P. Li, J. F. Wendelken, J. Shen, L. C. Feldman, J. R. Thompson, and H. H. Weitering, Phys. Rev. B **72**, 195205 (2005).
[3] D. Bougeard, S. Ahlers, A. Trampert, N. Sircar, and G. Abstreiter, Phys. Rev. Let. **97**, 237202 (2006).
[4] S. Ahlers, D. Bougeard, N. Sircar, G. Abstreiter, A. Trampert, M. Opel, and R. Gross, Phys. Rev. B **74**, 214411 (2006).
[5] L. Ottaviano, M. Passacantando, S. Picozzi, A. Continenza, R. Gunnella, A. Verna, G. Bihlmayer, G. Impellizzeri, and F. Priolo, Appl. PHys. Lett. **88**, 061907 (2006).
[6] S. Zhou, D. Bürger, M. Helm, and H. Schmidt, Appl. Phys. Lett. **95**, 172103 (2009).
[7] L. Ottaviano, A. Continenza, G. Profeta, G. Impellizzeri, A. Irrera, R. Gunnella, and O. Kazakova, Phys. Rev. B **83**, 134426 (2011).
[8] S. Zhou, D. Bürger, W. Skorupa, P. Oesterlin, M. Helm, and H. Schmidt, Appl. Phys. Lett. **96**, 202105 (2010).
[9] S. Zhou, D. Burger, A. Mucklich, C.Baumgart, W. Skorupa, C. Timm, P.Oesterlin, M. Helm, and H. Schmidt, Phys. Rev. B **81**, 165204 (2010).
[10] A. Portavoce, O. Abbes, Y. Rudzevich, L. Chow, V. L. Thanh, and C. Girardeaux, Scripta Materialia **67**, 269 (2012).
[11] M. M. Özer, J. R. Thompson, and H. H. Weitering, Phys. Rev. B **85**, 125208 (2012).
[12] I. G. Bucsa, R. W. Cochrane, and S. Roorda, J. Appl. Phys. **106**, 013914 (2009).
[13] B. C. Johnson, P. Gortmaker, and J. C. McCallum, Phys. Rev. B **77**, 214109 (2008).
[14] F. Ferri and A. Zanatta, J. Phys. D. **42**, 035005 (2009).
[15] T. Jungwirth and P. Horodyská, Phys. Rev. Lett. **105**, 227201 (2010).
[16] B. C. Chapler, S. Mack, R. C. Myers, A. Frenzel, B. C. Pursley, K. S. Burch, A. M. Dattelbaum, N. Samarth, D. D. Awschalom, and D. N. Basov, Phys. Rev. B **87**, 205314 (2012).
[17] D. W. Abraham, M. M. Frank, and S. Guha, Appl. Phys. Lett. **87**, 252502 (2005).
[18] G. Yang, G. Wang, W. Xiang, M. Khizar, Y. Guan, Y. Sun, D. Mei, C. Jiang, and B. Gray, in *Bulletin American Physical Society* (APS, Boston, 2012) bAPS.2012.MAR.A24.4.
[19] J. F. Ziegler, *The Stopping and Range of Ions in Matter Software* (www.srim.org, 2013).
[20] A. Continenza, G. Profeta, and S. Picozzi, Phy. Rev. B **73**, 035212 (2006).
[21] S. Koffel, N. Cherkashin, F. Houdellier, M. J. Hytch, G. Benassayag, P. Scheiblin, and A. Claverie, Journal of Applied Physics **105**, 126110 (2009).
[22] S. Zhou, W. Zhang, A. Shalimov, Y. Wang, Z. Huang, D. Buerger, A. Mücklich, W. Zhang, H. Schmidt, and M. Helm, Nanoscale Res. Lett. **7**, 528 (2012).
[23] O. Tosun, M. Salehi-Fashami, B. Balasubramanian, R. Skomski, D. J. Sellmyer, and G. C. Hadjipanayis, Nanomaterials **8**, 241 (2018).
[24] A. Stroppa, S. Picozzi, A. Continenza, and A. J. Freeman, Phys. Rev. B **68**, 155203 (2003).
[25] A. B. Kuzmenko, Rev. Sci. Inst. **76**, 083108 (2005).
[26] B. L. Frey, D. B. Leviton, and T. J. Madison, "*Temperature-dependent refractive index of silicon and germanium*," `https://ntrs.nasa.gov/archive/nasa/casi.ntrs.nasa.gov/20070021411.pdf` [Accessed: 08-07-2018].
[27] H. Phillip and E. Taft, Phys. Rev. **113**, 1002 (1958).
[28] H. Fuchs, C. H. Grein, M. Bauer, and M. Cardona, Phys. Rev. B **45**, 4065 (1992).
[29] M. Ikezawa and T. Nanba, J. Phys. Soc. Jpn. **45**, 148 (1978).
[30] M. L. Theye, Optics Communications **2**, 329 (1970).
[31] W. Prettl, N. J. Shevchik, and M. Cardona, phys. stat. sol. (b) **59**, 241 (1973).
[32] R. Stimets, J. Waldman, J. Lin, T. Chang, R. Temkin, and G. Connell, Sol. St. Com. **13**, 1485 (1973).
[33] J. Tauc, Mat. Res. Bull. **3**, 37 (1968).
[34] T. M. Donovan, W. E. Spicer, J. Bennet, and E. J. Ashley, Phys. Rev. B **2**, 397 (1970).
[35] G. E. Jellison and F. A. Modine, Appl. Phys. Lett. **69**, 371 (1996).
[36] G. E. Jellison and F. A. Modine, Appl. Phys. Lett. **69**, 2137 (1996).
[37] J. H. Selj, T. Mongstad, B. C. Hauback, and S. Z. Karazhanov, Thin Solid Films **520**, 6786 (2012).
[38] J. Tauc, R. Grigorovici, and A. Vancu, Phys. Stat. Sol. **15**, 627 (1966).
[39] W. C. Dash and R. Newman, Phys. Rev. **99**, 1151 (1955).
[40] M. H. Brodsky and A. Lurio, Phy. Rev. B **9**, 1646 (1974).
[41] R. Newman, H. H. Woodbury, and W. W. Tyler, Phys. Rev. **102**, 613 (1956).
[42] R. Newman and W. W. Tyler, Sol. St. Phys. **8**, 49 (1959).
[43] J. Pankove, *Optical Processes in Semiconductors* (New York: Dover, 1975).
[44] W. Kaiser, R. Collins, and H. Fan, Phys. Rev. **91**, 1380 (1953).
[45] L. Johnson and H. Levinstein, Phys. Rev. **117**, 1191 (1960).
[46] K. D. Cummings, J. C. Garland, and D. B.Tanner, Phys. Rev. B **30**, 4170 (1984).
[47] D. D. Nolte, J. Appl. Phys. **76**, 3740 (1994).
[48] D. Zhang, E. Cherkaev, and M. Lamoureux, Appl. Math. and Comp. **217**, 7092 (2011).
[49] S. S. A. Seo, T. W. Noh, Y.-W. Kim, J. Lim, Y. Park, Y. Kim, Z. Khim, H. C. Jeon, T. Kang, and S. Pearton, J. Appl. Phys. **95**, 8172 (2004).
[50] S. Dordevic, L. Kohlman, N. Stojilovic, R. Hu, and C. Petrovic, Phys. Rev. B **80**, 115114 (2009).
[51] `http://www.ioffe.ru/SVA/NSM/Semicond/Ge/index.htm` [Accessed: 06-06-2018].
[52] O. Golikova., B. Y. Moizhez, and L. S. Stilbans, Sov. Phys. Sol. St. **3**, 2259 (1962).